



OPEN

Penultimate deglaciation Asian monsoon response to North Atlantic circulation collapse

Jasper A. Wassenburg^{1,8,9}✉, Hubert B. Vonhof¹, Hai Cheng^{2,3,4}, Alfredo Martínez-García¹, Pia-Rebecca Ebner¹, Xianglei Li⁵, Haiwei Zhang^{1,2}, Lijuan Sha², Ye Tian^{1,2}, R. Lawrence Edwards⁵, Jens Fiebig^{1,6} and Gerald H. Haug^{1,7}

During glacial terminations, massive iceberg discharges and meltwater pulses in the North Atlantic triggered a shutdown of the Atlantic Meridional Overturning Circulation (AMOC). Speleothem calcium carbonate oxygen isotope records ($\delta^{18}\text{O}_{\text{cc}}$) indicate that the collapse of the AMOC caused dramatic changes in the distribution and variability of the East Asian and Indian monsoon rainfall. However, the mechanisms linking changes in the intensity of the AMOC and Asian monsoon $\delta^{18}\text{O}_{\text{cc}}$ are not fully understood. Part of the challenge arises from the fact that speleothem $\delta^{18}\text{O}_{\text{cc}}$ depends on not only the $\delta^{18}\text{O}$ of precipitation but also temperature and kinetic isotope effects. Here we quantitatively deconvolve these parameters affecting $\delta^{18}\text{O}_{\text{cc}}$ by applying three geochemical techniques in speleothems covering the penultimate glacial termination. Our data suggest that the weakening of the AMOC during meltwater pulse 2A caused substantial cooling in East Asia and a shortening of the summer monsoon season, whereas the collapse of the AMOC during meltwater pulse 2B (133,000 years ago) also caused a dramatic decrease in the intensity of the Indian summer monsoon. These results reveal that the different modes of the AMOC produced distinct impacts on the monsoon system.

The Asian monsoon provides fresh water for a densely populated region and plays a major role in global climate as a conveyor of latent and sensible heat¹. Changes in the cross-equatorial ocean energy transport driven by the Atlantic Meridional Overturning Circulation (AMOC) play a fundamental role in the monsoon system through its impact on the interhemispheric temperature gradient and the latitudinal position of the intertropical convergence zone (ITCZ)². A weaker AMOC also decreases sub-polar temperatures, which affect the course and strength of the westerly winds that interfere with southerly monsoon winds³. Palaeo-climate records offer a unique opportunity to study the links between changes in AMOC strength and the Asian monsoon system during periods of the past when the AMOC was substantially weaker or even completely collapsed^{4,5}, but there is no general consensus about the dominant mechanisms. Understanding the response of the monsoon system to rapid changes in the strength of the AMOC is particularly relevant in the context of recent observational evidence suggesting a weakening of the AMOC over the past decades^{6–9}.

The oxygen isotopic composition of speleothem calcite from East Asia suggests that rapid changes in the strength of the AMOC and the Asian monsoon were indeed tightly linked^{3,10–15}. During the coldest parts of the last glacial, that is, during Heinrich events, a weakening or collapse of the AMOC⁴ was systematically associated with higher speleothem $\delta^{18}\text{O}_{\text{cc}}$ (refs. ^{12,13,16}). Classically, higher speleothem $\delta^{18}\text{O}_{\text{cc}}$ values have been interpreted as ‘weak monsoon intervals’ and explained by a lower proportion of low $\delta^{18}\text{O}_{\text{p}}$ (Indian summer monsoon (ISM) and East Asian summer monsoon

(EASM)) rainfall in annual totals^{11,16,17} and or decreased upstream depletion of ^{18}O in either the ISM or East Asian monsoon (EAM) regions^{11,14,17,18}, and vice versa for low speleothem $\delta^{18}\text{O}_{\text{cc}}$ values, which are interpreted as ‘strong monsoon intervals’. However, with the available data, it is not possible to distinguish how the different components of the Asian monsoon system (for example, temperature gradients, the position of the ITCZ, the length of the monsoon season or the intensity of the ISM or EASM) are affected by changes in the strength of the AMOC.

Deconvolving calcite $\delta^{18}\text{O}$

Part of the challenge arises from the fact that $\delta^{18}\text{O}_{\text{cc}}$ depends on not only mean annual drip water $\delta^{18}\text{O}$ but also temperature-controlled isotope fractionation between water and calcite¹⁹, and potential kinetic isotope effects²⁰. Here, we use an innovative approach to deconvolve the effects of kinetic isotope fractionation, temperature and drip water $\delta^{18}\text{O}$ by combining: (i) the TEX_{86} speleothem thermometer to reconstruct changes in cave air temperatures^{21,22}, (ii) the dual clumped isotope (Δ_{47} and Δ_{48}) thermometer that allows to assess both changes in cave temperature and the extent of kinetic isotope fractionation^{23,24} and (iii) the hydrogen and oxygen isotope composition of speleothem fluid inclusions, that is, $\delta^3\text{H}_{\text{FI}}$ and $\delta^{18}\text{O}_{\text{FI}}$, as a proxy for the isotopic composition of precipitation, that is, $\delta^2\text{H}_{\text{p}}$ and $\delta^{18}\text{O}_{\text{p}}$ (refs. ^{25,26}). We applied these techniques to two south-west Chinese speleothems from Jiangjun Cave spanning the penultimate deglaciation²⁷ (Fig. 1 and Extended Data Figs. 1 and 2), a time period that was characterized by two successive episodes of vast freshwater discharge into the North Atlantic²⁸ (meltwater

¹Climate Geochemistry Department, Max Planck Institute for Chemistry, Mainz, Germany. ²Institute of Global Environmental Change, Xi'an Jiaotong University, Xi'an, China. ³State Key Laboratory of Loess and Quaternary Geology, Institute of Earth Environment, Chinese Academy of Sciences, Xi'an, China. ⁴Key laboratory of Karst Dynamics, MLR, Institute of Karst Geology, CAGS, Guilin, China. ⁵Department of Earth and Environmental Sciences, University of Minnesota, Tate Hall, Minneapolis, MN, USA. ⁶Institute of Geosciences, Goethe University, Frankfurt, Germany. ⁷Department of Earth Sciences, ETH Zürich, Zürich, Switzerland. ⁸Present address: Center for Climate Physics, Institute for Basic Science, Busan, Republic of Korea. ⁹Present address: Pusan National University, Busan, Republic of Korea. ✉e-mail: jasper.wassenburg@pusan.ac.kr

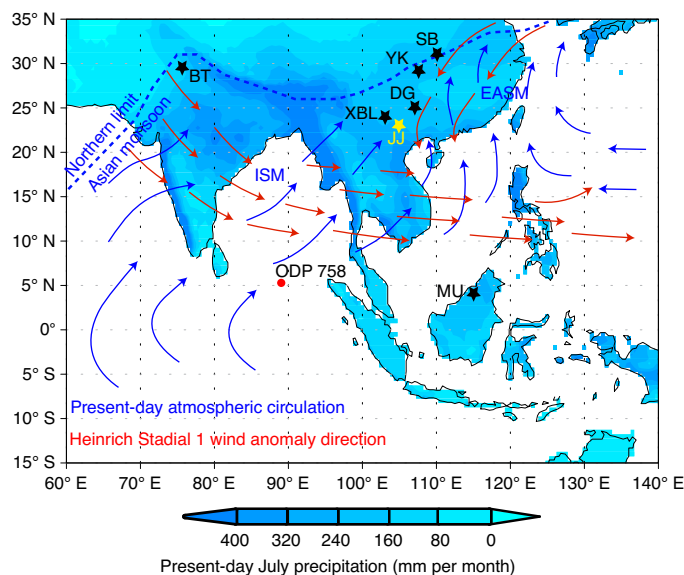


Fig. 1 | Locations of the cave sites. The locations of the cave sites discussed in the main text: Jiangjun Cave (JJ; this study; yellow star; 200 m above sea level; 22° 57' N 104° 49' E; Extended Data Fig. 1), Dongge Cave (DG), Xiaobailong Cave (XBL), Yangkou Cave (YK), Sanbao Cave (SB), Bittoo Cave (BT) and the Mulu cave record (MU; black stars) in relation to main atmospheric circulation patterns, northern limit of the Asian monsoon and precipitation in July during the present day (1901–2016), and Ocean Drilling Program (ODP) 758 core site (red dot). Red arrows show the direction of 850 mB wind anomalies during a full shutdown of the AMOC associated with HS1 after ref. ³.

pulses (MWP) that caused a weakening²⁹ (MWP 2A) and full collapse (MWP 2B) of the AMOC⁴.

The present-day local climate at Jiangjun Cave is characterized by warm/wet summers and cold/dry winters. The summer monsoon peaks from May to September³⁰, contributing ~73% to annual rainfall (~1,320 mm per year), and the mean annual air temperature is ~23 °C. Wet-season (summer) precipitation in the region of Jiangjun correlates positively with precipitation in north-east India, which, in turn, depends on the strength of the ISM³¹. Consequently, Jiangjun $\delta^{18}\text{O}_p$ is about 10‰ lower in July–August compared with January–March (Extended Data Fig. 3).

Structure of Termination II

During the penultimate deglaciation, Jiangjun $\delta^{18}\text{O}_{cc}$ (Supplementary Data Table 1a) shows trends similar to those found in Sanbao Cave $\delta^{18}\text{O}_{cc}$ (and other EAM records; Extended Data Fig. 4). From 151 to 130 ka, two positive shifts are observed in all EAM records, superimposed on a gradual trend towards higher $\delta^{18}\text{O}_{cc}$ (Fig. 2a). The first occurred around ~139 ka (1‰), synchronous with MWP 2A. The second shift occurred at ~136 ka (2‰; Fig. 2), within dating error of the onset of MWP 2B²⁸ (135 ± 1 ka) and Heinrich Stadial (HS) 11. After this event, $\delta^{18}\text{O}_{cc}$ remains stable with the exception of the small Termination II (TII) interstadial peak at ~134 ka. At the end of the glacial termination (~130 ka), Jiangjun $\delta^{18}\text{O}_{cc}$ shows a 7‰ shift towards lower $\delta^{18}\text{O}_{cc}$, whereas Sanbao shifts by only 4‰. The 7‰ shift at Jiangjun replicates the $\delta^{18}\text{O}_{cc}$ change at the nearby Xiaobailong Cave³¹, while the 4‰ shift at Sanbao is consistent with those found in Dongge and Yangkou caves located north-east of Jiangjun, suggesting a greater influence of ISM precipitation in south-west China (Fig. 1 and Extended Data Fig. 4).

The structure of the Jiangjun $\delta^{18}\text{O}_{cc}$ record is similar to our TEX₈₆ temperatures. We observe a long-term cooling from 144 to

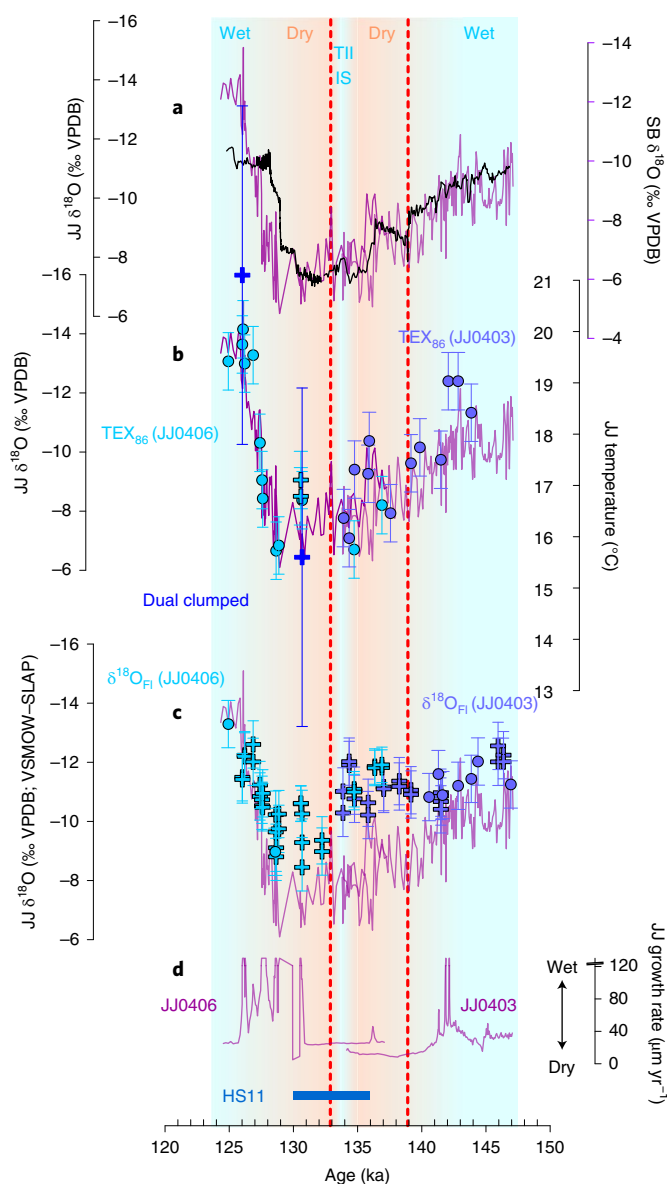


Fig. 2 | Jiangjun proxy data. **a, b**, Jiangjun (JJ) $\delta^{18}\text{O}_{cc}$ (JJ0406, JJ0403; violet)²⁷ with respect to Sanbao (SB) EAM $\delta^{18}\text{O}_{cc}$ ³¹ (black) (**a**) and JJ0406 (light blue) and JJ0403 (purple) TEX₈₆ and dual clumped temperatures (blue) (**b**). **c**, JJ0406 (light blue) and JJ0403 (purple) $\delta^{18}\text{O}_{Fi}$. **d**, Speleothem growth rates. Peach shading indicates the main dry phase as based on speleothem growth rates interrupted by the short Termination II (TII) interstadial around 134 ka. Blue shading indicates wet periods. Uncertainties shown in **b** are 2 s.d. for TEX₈₆ and error propagated 2 s.e. for clumped isotope data (Methods). Uncertainties in **c** are 2 s.d. (Methods). Timings of Heinrich Stadial 11 (ref. ²⁹) (HS11, blue bar) and MWP 2A around 139 ka and 2B around 133 ka (red dashed lines) are indicated. In **b** and **c**, crosses indicate sample replicates while round symbols indicate samples without replicates.

135 ka of about 3 °C. Superimposed on this cooling trend, an additional cooling of around 1 °C occurs during MWP 2A (Fig. 2b and Supplementary Data Table 1b). After MWP 2A, temperatures rise by around 1 °C, coinciding with an increase in $\delta^{18}\text{O}_{cc}$, and subsequently decrease by ~2 °C at the beginning of HS11. During the last part of the glacial termination, after ~130 ka, TEX₈₆ temperatures increase abruptly by 4 °C. These temperatures are consistent within uncertainty with the temperature estimates based on dual clumped

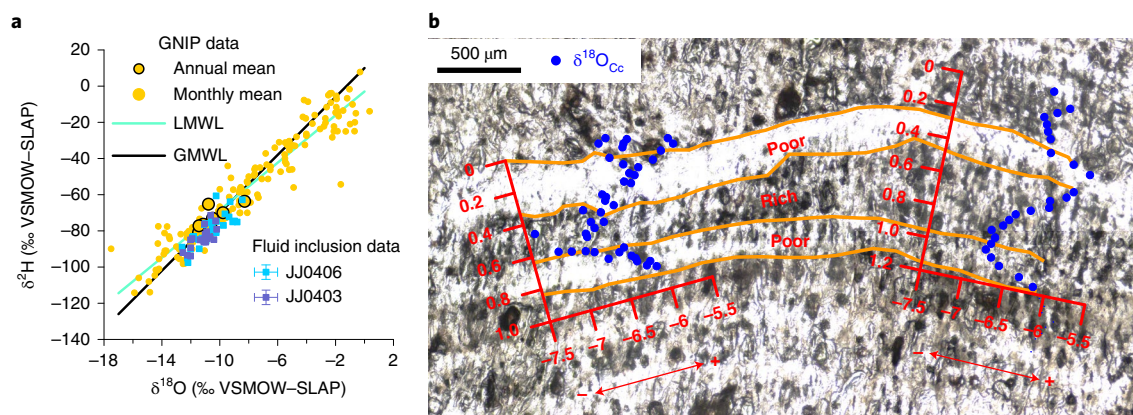


Fig. 3 | Fluid inclusion isotope composition and distribution. **a**, Local meteoric rainfall $\delta^{18}\text{O}$ and $\delta^2\text{H}$ data from Global Network of Isotopes in Precipitation (GNIP) station Kunming in the vicinity of Jiangjun with respect to the local and global meteoric water line (LMWL and GMWL) and the speleothem fluid inclusion data. Two s.d. is indicated. See Supplementary Data Table 1h for full details on station codes, coordinates and references. **b**, Optical microscopy image of speleothem JJ0406, showing the distribution of fluid inclusions in uncrushed material from fluid inclusion sample JJ0406-628 from MIS6 with respect to high-resolution $\delta^{18}\text{O}_{\text{Cc}}$ (blue). The y axis represents distance in millimetres. The x axis represents $\delta^{18}\text{O}_{\text{Cc}}$ with respect to VPDB. Fluid inclusion-poor layers are associated with higher $\delta^{18}\text{O}_{\text{Cc}}$, and vice versa for fluid inclusion-rich layers. The section is 250 μm thick, which is necessary to retrieve enough material for C and O isotope analysis but less ideal to present the speleothem fabric (Extended Data Fig. 1).

isotope data (Fig. 2b and Supplementary Data Tables 1c–f). In addition, our dual clumped isotope data show that calcite precipitated indistinguishable from isotope equilibrium (Extended Data Fig. 5). Applying a temperature-dependent water–calcite isotope fractionation of $0.21\text{‰}/1^\circ\text{C}$ (ref. ³³), we estimate the contribution of temperature to the changes observed in the $\delta^{18}\text{O}_{\text{Cc}}$ record. This calculation reveals that cave air temperature can only explain a small fraction of the variability observed in the $\delta^{18}\text{O}_{\text{Cc}}$ record, for example, only about 0.63‰ of the near 4‰ change in $\delta^{18}\text{O}_{\text{Cc}}$ from 144 to 135 ka, or about 0.84‰ of the 7‰ change observed during the last part of the deglaciation after ~ 130 ka. Therefore, our data demonstrate that changes in $\delta^{18}\text{O}_{\text{Cc}}$ are mainly dominated by variations in annual mean parent water $\delta^{18}\text{O}$ (Extended Data Fig. 6).

However, in contrast to $\delta^{18}\text{O}_{\text{Cc}}$, Jiangjun $\delta^{18}\text{O}_{\text{Fi}}$ shows no response to MWP 2A. An abrupt shift towards more positive $\delta^{18}\text{O}_{\text{Fi}}$ is only observed around 133 ka, coinciding with the peak of MWP 2B (Fig. 2 and Supplementary Data Table 1g). One potential explanation for these differences could be that the fluid inclusions are not well preserved and do not represent palaeo-rainfall. A key criterion to assess this is that, if unaltered, the fluid inclusion isotope data should plot close to the local and global meteoric water line³³. For Jiangjun Cave, the most representative Global Network of Isotopes in Precipitation data are from Kunming, which are highly consistent with the fluid inclusion data (Fig. 3a). Furthermore, Jiangjun's interglacial $\delta^{18}\text{O}_{\text{Fi}}$ values are very similar to values calculated for parent drip water based on Jiangjun's TEX_{86} and dual clumped isotope temperatures and the $\delta^{18}\text{O}$ temperature calibration from ref. ³⁴, which bolsters the quality of our dataset (Extended Data Fig. 6). The fluid inclusions are thus well preserved and represent the isotopic composition of the parent water.

Closer examination of our dataset revealed a $\sim 1\text{--}3\text{‰}$ offset between parent water $\delta^{18}\text{O}$ (calculated by subtracting the temperature contribution from calcite $\delta^{18}\text{O}$) and $\delta^{18}\text{O}_{\text{Fi}}$ from ~ 139 to ~ 128 ka, with $\delta^{18}\text{O}_{\text{Fi}}$ being lower than calculated parent water values (Extended Data Fig. 6). Since this offset occurs in the overlap zone of the two speleothems where $\delta^{18}\text{O}_{\text{Cc}}$, $\delta^{18}\text{O}_{\text{Fi}}$ and TEX_{86} proxy records replicate well, we do not believe that this reflects kinetic fractionation or diagenetic processes. We propose instead that, in this interval, the difference arises because $\delta^{18}\text{O}_{\text{Fi}}$ is seasonally biased, mainly capturing the $\delta^{18}\text{O}$ of intense ISM rainfall events, while $\delta^{18}\text{O}_{\text{Cc}}$ captures the annually averaged signal (Supplementary

Information and Fig. S1). Our microscale analysis of the speleothem fabric and $\delta^{18}\text{O}_{\text{Cc}}$ indeed reveal an inhomogeneous distribution of fluid inclusions during glacial times, characterized by an alternation of fluid inclusion-poor layers (associated with higher $\delta^{18}\text{O}_{\text{Cc}}$) and fluid inclusion-rich layers (associated with lower $\delta^{18}\text{O}_{\text{Cc}}$) (Fig. 3b). The low $\delta^{18}\text{O}_{\text{Cc}}$ values found in the fluid inclusion-rich laminae are associated with the ISM season (which is characterized by low $\delta^{18}\text{O}_{\text{p}}$). These data suggest that, during the driest part of the glacial period, characterized by low speleothem growth rates (Fig. 2d) and a less developed soil on top of the cave, strong monsoon rainfall events infiltrated rapidly and were captured in fluid inclusion-rich calcite laminae. In the dry season, fluid inclusion-poor laminae were formed, causing a distinct seasonal bias in fluid inclusion incorporation, while the calcite grew in both wet and dry seasons³⁵ (Fig. 3b). This effectively decouples $\delta^{18}\text{O}_{\text{Fi}}$ and $\delta^{18}\text{O}_{\text{Cc}}$ records, and highlights that $\delta^{18}\text{O}_{\text{Fi}}$ predominantly captures the strength or 'intensity' of the ISM that integrates the rainfall history along the moisture pathway, while $\delta^{18}\text{O}_{\text{Cc}}$ values are more likely to reflect the annually averaged hydroclimate signal.

Implications for monsoon dynamics

Our data indicate that MWP 2A did not affect $\delta^{18}\text{O}_{\text{Fi}}$ but did affect temperature and $\delta^{18}\text{O}_{\text{Cc}}$, so how can this be reconciled? MWP 2A was associated with a peak in ice-rafted debris³⁶ (IRD) in the North Atlantic and caused a weakening of the AMOC as observed in benthic $\delta^{13}\text{C}$ values (ref. ²⁹) (Fig. 4). Two additional IRD peaks of similar magnitude have been observed before and after MWP 2A, also associated with benthic $\delta^{13}\text{C}$ minima, suggesting multiple periods of weakening and reinvigoration of the AMOC during this time period. A weakening of the AMOC leads to cooling in the subpolar North Atlantic, which increases the equator-to-pole temperature gradient and triggers a southward shift of the westerly jet, as shown by climate simulations of HS1 (ref. ³). Interestingly, our speleothem TEX_{86} temperature record shows three cooling events (of $\sim 1^\circ\text{C}$) in south-west China that occur within age uncertainties of these North Atlantic IRD events (Fig. 4). However, MWP 2A, as well as the two additional IRD events, were likely too small to induce a complete shutdown of the AMOC. Consequently, ocean-to-continent temperature gradients were likely not affected to the extent that they impacted the strength of the ISM, as suggested by the relatively stable Jiangjun $\delta^{18}\text{O}_{\text{Fi}}$ values during this period. This interpretation

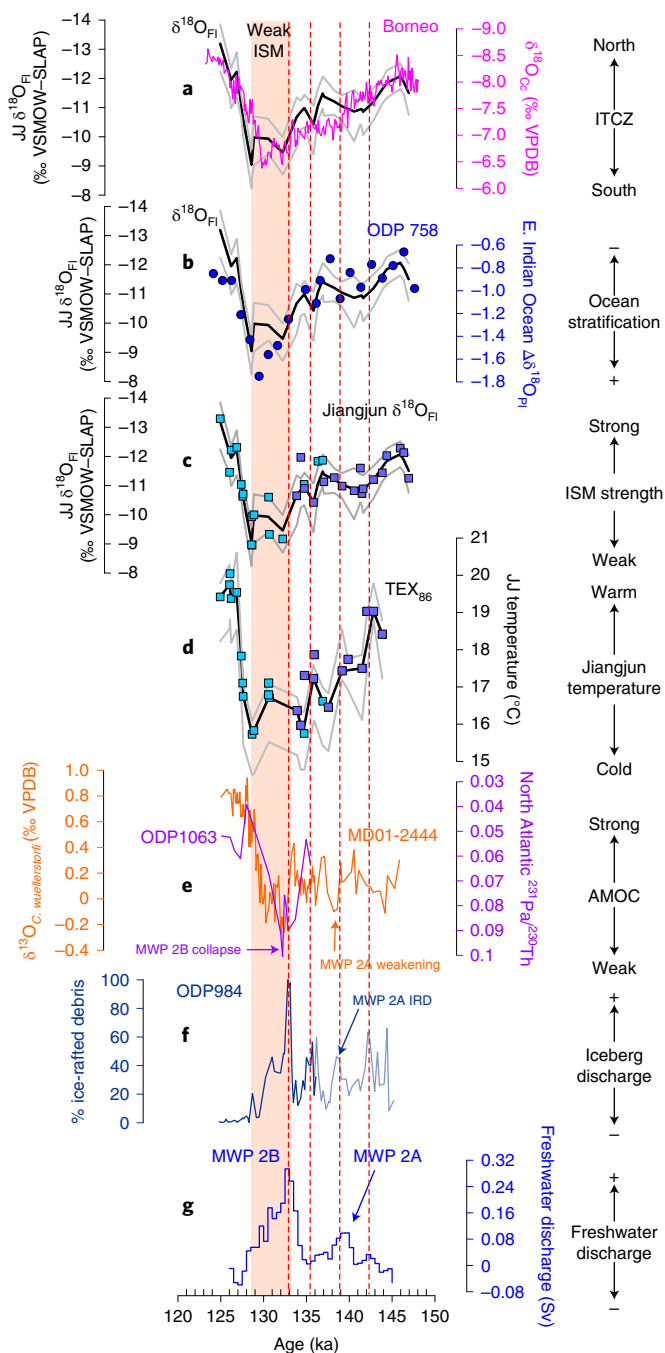


Fig. 4 | Climatic context of Jiangjun proxy data. a–g, Jiangjun $\delta^{18}\text{O}_{\text{FI}}$ (**c**) and TEX_{86} temperature (**d**) with smoothed loess curve (black) and 95% confidence limits (grey); replicate samples were averaged to obtain a single value for ease of visualization of the millennial timescale trends. Trend of Jiangjun $\delta^{18}\text{O}_{\text{FI}}$ (black) versus Mulu $\delta^{18}\text{O}_{\text{Cc}}$ from Borneo³⁹ (magenta; **a**) and upper ocean stratification from the eastern equatorial Indian Ocean³⁷ (blue; **b**). North Atlantic benthic foraminifera (*Cibicides wuellerstorfi*) $\delta^{13}\text{C}$ on the Corchia speleothem timescale²⁹ (orange) and $^{231}\text{Pa}/^{230}\text{Th}$ (ref. 4, purple; **e**). North Atlantic IRD record³⁶ on the Corchia speleothem timescale²⁹ from 136.1 to 124.8 ka and original timescale between 145 and 136.1 ka (navy blue; **f**) and freshwater discharge based on Red Sea sea level rise rates on the Soreq speleothem timescale²⁸ (blue; **g**). The onset of the weakest phase of the Indian summer monsoon (ISM) is coincident with the timing of MWP 2B in the North Atlantic. Timings of IRD events and MWPs around 142, 139, 136 and 133 ka are indicated by dashed red lines.

is supported by the high correlation ($r = -0.74$, $P < 0.001$, $n = 17$) between $\delta^{18}\text{O}_{\text{FI}}$ and independent marine reconstructions of the ISM wind-induced upper ocean stratification in the east equatorial Indian Ocean³⁷, which suggest a weak response of the ISM wind strength to MWP 2A and surrounding MWP events (Fig. 4). Despite this apparent lack of response of the ISM intensity, a clear signal is observed in the $\delta^{18}\text{O}_{\text{Cc}}$ records during MWP 2A and the onset of MWP 2B that cannot be explained by the observed temperature change alone, suggesting a change in annual mean $\delta^{18}\text{O}_{\text{p}}$. We hypothesize that these observations can be reconciled if the timing of the northward retreat of the westerly jet in the Asian monsoon region was delayed in response to the enhanced equator-to-pole temperature gradient, shortening the monsoon season in a similar fashion as during HS1 (ref. 3). In agreement with climate simulations³ and Jiangjun speleothem growth rate (Fig. 2), this scenario would have resulted in a decrease in annual mean precipitation at Jiangjun during this interval (Fig. 2d). The consequences of a delayed northward retreat of the westerly jet would have been similar in northern India and in the Arabian Peninsula, causing also a shortening of the monsoon season and thus more positive annual mean parent water $\delta^{18}\text{O}$. More dominant westerlies also brought ^{18}O -enriched water vapour from the Mediterranean to the Arabian Peninsula³⁸, supporting our hypothesis. The small southward shift of the ITCZ as indicated by the Mulu $\delta^{18}\text{O}_{\text{Cc}}$ record³⁹ (Fig. 4) is in agreement with a moderate southward shift of the westerly jet. Thus, our interpretation represents a viable mechanism to explain the consistency of speleothem $\delta^{18}\text{O}_{\text{Cc}}$ across the Asian monsoon region, as well as their apparent discrepancy with the available ISM records.

In contrast to MWP 2A, MWP 2B was associated with massive iceberg discharge events in the North Atlantic and a full shutdown of the AMOC, as shown by the kinematic AMOC tracer $^{231}\text{Pa}/^{230}\text{Th}$ (Fig. 4e). Our data reveal that MWP 2B was characterized by colder temperatures and a dramatic decrease in the intensity of the ISM (reflected in a 2–3‰ increase in $\delta^{18}\text{O}_{\text{FI}}$; Figs. 2 and 4). These changes coincide with a maximum in planktonic foraminifera surface-to-thermocline $\delta^{18}\text{O}$ gradients in the southernmost Bay of Bengal (Fig. 4b). The role of sea surface temperature in the Bay of Bengal during Heinrich events has not been resolved yet⁴⁰, but climate model simulations of HS1 suggest that, as opposed to the Arabian Sea, sea surface temperature did not change significantly in that region (see fig. S4 in ref. 15), suggesting that the increase in the planktonic foraminifera gradients reflects a strengthening of ocean stratification in response to a weaker ISM wind strength. Our data provide empirical support for this interpretation. In addition, the timing and structure of our $\delta^{18}\text{O}_{\text{FI}}$ mirror the Mulu cave $\delta^{18}\text{O}_{\text{Cc}}$ record, suggesting that the weakening of the ISM during MWP 2B was closely coupled to the migration of the ITCZ towards its southernmost position (Fig. 4a). Thus, our data suggest that the strong Northern Hemisphere cooling associated with the collapse of the AMOC during MWP 2B affected both the ocean-to-continent and the equator-to-pole temperature gradients, impacting both the intensity of the ISM and the length of the monsoon season.

These results underpin the potential of using multiple analytical techniques to quantitatively deconvolve the different components affecting speleothem $\delta^{18}\text{O}_{\text{Cc}}$. Our $\delta^{18}\text{O}_{\text{FI}}$ record suggests that the intensity of the ISM only decreased substantially with the full shutdown of the AMOC during the peak of MWP 2B, which was associated with an extreme southward migration of the ITCZ. In contrast, smaller AMOC reductions associated with earlier North Atlantic IRD events, including MWP 2A, appeared to have impacted atmospheric temperatures and reduced the length of the monsoon season (as suggested by $\delta^{18}\text{O}_{\text{Cc}}$ records), but did not affect the intensity of the ISM substantially. Thus, our data indicate a distinct response of the Asian monsoon system to changes in the strength of the AMOC.

Online content

Any methods, additional references, Nature Research reporting summaries, source data, extended data, supplementary information, acknowledgements, peer review information; details of author contributions and competing interests; and statements of data and code availability are available at <https://doi.org/10.1038/s41561-021-00851-9>.

Received: 17 September 2020; Accepted: 1 October 2021;

Published online: 18 November 2021

References

- Mohtadi, M., Prange, M. & Steinke, S. Palaeoclimatic insights into forcing and response of monsoon rainfall. *Nature* **533**, 191–199 (2016).
- Schneider, T., Bischoff, T. & Haug, G. H. Migrations and dynamics of the intertropical convergence zone. *Nature* **513**, 45–53 (2014).
- Zhang, H. et al. East Asian hydroclimate modulated by the position of the westerlies during Termination I. *Science* **362**, 580–583 (2018).
- Böhm, E. et al. Strong and deep Atlantic Meridional Overturning Circulation during the last glacial cycle. *Nature* **517**, 73–76 (2015).
- McManus, J. F., Francois, R., Gherardi, J. M., Keigwin, L. D. & Brown-Leger, S. Collapse and rapid resumption of Atlantic meridional circulation linked to deglacial climate changes. *Nature* **428**, 834–837 (2004).
- Caesar, L., Rahmstorf, S., Robinson, A., Feulner, G. & Saba, V. Observed fingerprint of a weakening Atlantic Ocean overturning circulation. *Nature* **556**, 191–196 (2018).
- Thornalley, D. J. R. et al. Anomalously weak Labrador Sea convection and Atlantic overturning during the past 150 years. *Nature* **556**, 227–230 (2018).
- Srokosz, M. A. & Bryden, H. L. Observing the Atlantic Meridional Overturning Circulation yields a decade of inevitable surprises. *Science* **348**, 1255575 (2015).
- Golledge, N. R. et al. Global environmental consequences of twenty-first-century ice-sheet melt. *Nature* **566**, 65–72 (2019).
- Cheng, H. et al. Ice age terminations. *Science* **326**, 248–252 (2009).
- Cheng, H. et al. The Asian monsoon over the past 640,000 years and ice age terminations. *Nature* **534**, 640–646 (2016).
- Cheng, H. et al. Atmospheric $^{14}\text{C}/^{12}\text{C}$ changes during the last glacial period from Hulu Cave. *Science* **362**, 1293–1297 (2018).
- Kathayat, G. et al. Indian monsoon variability on millennial-orbital timescales. *Sci. Rep.* **6**, 24374 (2016).
- Pausata, F. S. R., Battisti, D. S., Nisancioglu, K. H. & Bitz, C. M. Chinese stalagmite $\delta^{18}\text{O}$ controlled by changes in the Indian monsoon during a simulated Heinrich event. *Nat. Geosci.* **4**, 474–480 (2011).
- Tierney, J. E., Pausata, F. S. R. & deMenocal, P. Deglacial Indian monsoon failure and North Atlantic stadials linked by Indian Ocean surface cooling. *Nat. Geosci.* **9**, 46–50 (2016).
- Wang, Y. J. et al. A high-resolution absolute-dated Late Pleistocene monsoon record from Hulu Cave, China. *Science* **294**, 2345–2348 (2001).
- Orland, I. J. et al. Direct measurements of deglacial monsoon strength in a Chinese stalagmite. *Geology* **43**, 555–558 (2015).
- Yuan, D. X. et al. Timing, duration, and transitions of the Last Interglacial Asian monsoon. *Science* **304**, 575–578 (2004).
- Lachniet, M. S. Climatic and environmental controls on speleothem oxygen-isotope values. *Quat. Sci. Rev.* **28**, 412–432 (2009).
- Hansen, M., Scholz, D., Schöne, B. R. & Spötl, C. Simulating speleothem growth in the laboratory: determination of the stable isotope fractionation ($\delta^{13}\text{C}$ and $\delta^{18}\text{O}$) between H_2O , DIC and CaCO_3 . *Chem. Geol.* **509**, 20–44 (2019).
- Baker, A. et al. Glycerol dialkyl glycerol tetraethers (GDGT) distributions from soil to cave: refining the speleothem paleothermometer. *Org. Geochem.* **136**, 103890 (2019).
- Blyth, A. J. & Schouten, S. Calibrating the glycerol dialkyl glycerol tetraether temperature signal in speleothems. *Geochim. Cosmochim. Acta* **109**, 312–328 (2013).
- Fiebig, J. et al. Combined high-precision Δ_{48} and Δ_{47} analysis of carbonates. *Chem. Geol.* **522**, 186–191 (2019).
- Fiebig, J. et al. Calibration of the dual clumped isotope thermometer for carbonates. *Geochim. Cosmochim. Acta* <https://doi.org/10.1016/j.gca.2021.07.012> (2021).
- van Breukelen, M. R., Vonhof, H. B., Hellstrom, J. C., Wester, W. C. G. & Kroon, D. Fossil dripwater in stalagmites reveals Holocene temperature and rainfall variation in Amazonia. *Earth Planet. Sci. Lett.* **275**, 54–60 (2008).
- de Graaf, S. et al. A comparison of IRMS and CRDS techniques for isotope analysis of fluid inclusion water. *Rapid Commun. Mass Spectrom.* **34**, e8837 (2020).
- Liu, G. et al. On the glacial–interglacial variability of the Asian monsoon in speleothem $\delta^{18}\text{O}$ records. *Sci. Adv.* **64**, eaay8189 (2020).
- Marino, G. et al. Bipolar seesaw control on Last Interglacial sea level. *Nature* **522**, 197–201 (2015).
- Tzedakis, P. C. et al. Enhanced climate instability in the North Atlantic and southern Europe during the Last Interglacial. *Nat. Commun.* **9**, 4235 (2018).
- Zhang, H. et al. Effect of precipitation seasonality on annual oxygen isotopic composition in the area of spring persistent rain in southeastern China and its paleoclimatic implication. *Clim. Past* **16**, 211–225 (2020).
- Cai, Y. et al. Variability of stalagmite-inferred Indian monsoon precipitation over the past 252,000 y. *Proc. Natl Acad. Sci. USA* **112**, 2954–2959 (2015).
- Johnston, V. E., Borsato, A., Spotl, C., Frisia, S. & Miorandi, R. Stable isotopes in caves over altitudinal gradients: fractionation behaviour and inferences for speleothem sensitivity to climate change. *Clim. Past* **9**, 99–118 (2013).
- Uemura, R., Kina, Y., Shen, C. C. & Omine, K. Experimental evaluation of oxygen isotopic exchange between inclusion water and host calcite in speleothems. *Clim. Past* **16**, 17–27 (2020).
- Daëron, M. et al. Most Earth-surface calcites precipitate out of isotopic equilibrium. *Nat. Commun.* **10**, 429 (2019).
- Brook, G. A., Rafter, M. A., Railsback, L. B., Sheen, S.-W. & Lundberg, J. A high-resolution proxy record of rainfall and ENSO since AD 1550 from layering in stalagmites from Anjohibe Cave. *Madag. Holocene* **9**, 695–705 (1999).
- Mokeddem, Z., McManus, J. F. & Oppo, D. W. Oceanographic dynamics and the end of the Last Interglacial in the subpolar North Atlantic. *Proc. Natl Acad. Sci. USA* **111**, 11263–11268 (2014).
- Bolton, C. T. et al. A 500,000-year record of Indian summer monsoon dynamics recorded by eastern equatorial Indian Ocean upper water-column structure. *Quat. Sci. Rev.* **77**, 167–180 (2013).
- Fleitmann, D., Burns, S. J., Neff, U., Mangini, A. & Matter, A. Changing moisture sources over the last 330,000 years in northern Oman from fluid-inclusion evidence in speleothems. *Quat. Res.* **60**, 223–232 (2003).
- Carolin, S. A. et al. Northern Borneo stalagmite records reveal West Pacific hydroclimate across MIS 5 and 6. *Earth Planet. Sci. Lett.* **439**, 182–193 (2016).
- Lauterbach, S. et al. An ~130 kyr record of surface water temperature and $\delta^{18}\text{O}$ from the northern Bay of Bengal: investigating the linkage between Heinrich events and weak monsoon intervals in Asia. *Paleoclimatol.* **35**, e2019PA003646 (2020).

Publisher's note Springer Nature remains neutral with regard to jurisdictional claims in published maps and institutional affiliations.



Open Access This article is licensed under a Creative Commons Attribution 4.0 International License, which permits use, sharing, adaptation, distribution and reproduction in any medium or format, as long as you give appropriate credit to the original author(s) and the source, provide a link to the Creative Commons license, and indicate if changes were made. The images or other third party material in this article are included in the article's Creative Commons license, unless indicated otherwise in a credit line to the material. If material is not included in the article's Creative Commons license and your intended use is not permitted by statutory regulation or exceeds the permitted use, you will need to obtain permission directly from the copyright holder. To view a copy of this license, visit <http://creativecommons.org/licenses/by/4.0/>.

© The Author(s) 2021

Methods

Stalagmite samples. The speleothems were collected from Jiangjun's main passage, which has a length of 4 km, height of 1.5–20 m and width of 3–25 m. The speleothems were collected ~2.8 km from the main entrance. The surface above the cave is densely vegetated during the summer season. The main entrance is covered by ~80 m of host rock.

Stalagmite JJ0406 from Jiangjun Cave is 860 mm long and grew 460 mm from 139 to 124 ka, JJ0403 is 485 mm long and grew 348 mm from 147 to 134 ka. JJ0406 shows a pool-type structure at the growth axis, which we avoided when sampling for fluid inclusions and $^{230}\text{Th}/\text{U}$ dating. We show a thin section of primary calcite with clear continuous lamination that corresponds to the fabric from which fluid inclusion samples were taken (Extended Data Fig. 1). The speleothem calcite $\delta^{18}\text{O}$ records were already published²⁷. There is a second Jiangjun Cave in south-west China⁴¹, which should not be confused with the Jiangjun Cave from this manuscript.

Uncrushed samples for fluid inclusion isotope analysis encompass ~5–20 mm of stratigraphy at the growth axis and thus represent about 50–200 years with a speleothem growth rate of 100 μm per year, or more with lower growth rates. Therefore, the fluid inclusion isotope record tracks ISM strength on multi-decadal to centennial timescales.

$^{230}\text{U}/\text{Th}$ dating and age–depth modelling. A total of 29 and 11 $^{230}\text{Th}/\text{U}$ datings were conducted on stalagmite JJ0406 and JJ0403, respectively (Supplementary Data Table 1a). Per sample, between 200 and 300 mg carbonate powder was used. Uranium and Th were chemically separated following a protocol adapted after ref. ⁴² and were measured using the technique described in ref. ⁴³. We used U decay constants as in refs. ^{43,44}. JJ0406 and JJ0403 contain only 20 ppb U, and $^{234}\text{U}/^{238}\text{U}_{\text{initial}}$ atomic ratios are low. These stalagmites are thus rather difficult to date, which resulted in relatively large age uncertainties (Supplementary Data Table 1a). Part of the U series ages of speleothem JJ0406 were recently published²⁷, being consistent with new U-series ages produced for this study. Age–depth modelling was performed using the StalAge algorithm⁴⁵ (Extended Data Fig. 2).

Carbonate oxygen isotope analysis. The oxygen and carbon isotope records of stalagmites JJ0403 and JJ0406 were constructed in the Xi'an Jiaotong Isotope Laboratory. Oxygen isotopes were published in ref. ²⁷. A total of 284 subsamples were drilled from speleothem JJ0403, every 1 mm for the top 190 mm and every 2 mm below 190 mm. Meanwhile, 172 subsamples were drilled from speleothem JJ0406 every 5 mm. The stable isotope analyses were conducted in the Isotope Laboratory of Xi'an Jiaotong University on a Finnigan–MAT 253 mass spectrometer connected with a Kiel Carbonate Device IV. Oxygen isotope ratios are reported relative to the Vienna Pee Dee Belemnite (VPDB) standard. The international standard TTB1 was added to the analysis every 10–20 samples to check the reproducibility of results. Results show analytical errors (1 s.d.) of 0.06‰. The carbon and oxygen isotope data are presented in Supplementary Data Table 1a.

The crushed calcite powders were analysed at the Max Planck Institute for Chemistry in Mainz, on a Thermo Delta V mass spectrometer equipped with a GASBENCH preparation device. A CaCO_3 sample (~20–50 μg) in a He-filled 12 ml extainer vial was digested in >99% H_3PO_4 at 70 °C. Subsequently the CO_2 –He gas mixture was transported to the GASBENCH in helium carrier gas. In the GASBENCH, water vapour and various gaseous compounds were separated from the He– CO_2 mixture before sending it to the mass spectrometer in nine separate peaks. Isotope values of these individual peaks were averaged and are reported as $\delta^{18}\text{O}$ relative to VPDB. A total of 20 replicates of two in-house CaCO_3 standards were analysed in each run of 55 samples. CaCO_3 standard weights were chosen such that they span the entire range of sample weights of the samples. The reproducibility of these standards is typically better than 0.1‰ (1 s.d.) for $\delta^{18}\text{O}$. The oxygen isotope data of the crush residues are presented in Supplementary Data Table 1g.

High-resolution sampling on the thick section of sample JJ0406-690 was performed with a micromill at 20 and 40 μm resolution using a pointy-tipped drill bit. Approximately 3–5 μg of carbonate was analysed with a cold-trap method connected to the setup described above (see ref. ⁴⁶ for more information). The oxygen isotope data are presented in Supplementary Data Table 1a.

Fluid inclusion isotope analysis. Stalagmites were sampled for fluid inclusion isotope analysis (Supplementary Data Table 1g) using a handheld device (Dremel Micro), equipped with a 20–38 mm diameter diamond-covered circular saw. Depending on the water content of the calcite, we cut small calcite blocks of 0.1–1.1 g per analysis. Fluid inclusion isotope analysis was performed following the protocols adapted after ref. ²⁶ using a Delta V advantage mass spectrometer (MS) coupled to a Conflow IV and a Thermo Conversion Element Analyser (TC-EA) from Thermo Scientific or an online preparation line coupled to a Picarro L2140i cavity ring-down spectrometer (CRDS). The calcite was crushed by a downward rotary movement in a Potsdam-type crusher⁴⁷ at a temperature of 120 °C. In ref. ²⁶, aliquots of the same samples were analysed with both techniques repeatedly. The results were consistent, proving that the techniques can be used interchangeably. In between samples, the crusher was cleaned with acetic acid and milliQ water and subsequently dried with pressurized air.

For the MS set-up, the water vapour is transported with He carrier gas to a cold trap at –105 °C. Water is trapped for 6 min, then flash-heated and transported to the TC-EA^{26,48}. We used a standard bracketing approach with an evaluation procedure to correct for signal intensity, memory and non-linearity effects²⁶. Memory and non-linearity effects of the set-up were assessed on a weekly basis following ref. ²⁶. By choosing a water standard with an isotope composition that is within a few ‰ of the fluid inclusions, the memory effect was minimized. To correct for signal intensity, a series of at least three standard waters were analysed before the crush, with water amounts ranging from 0.28 to 0.12 μL . After the crush, two or three injections of 0.4 μL of standard water were injected to flush the system, which was followed by one standard water analysis, which was not used for the data evaluation because it may still be affected by a potential memory effect related to the fluid inclusions from the crushed calcite. A minimum of another two water standards with water amounts similar to the crush were analysed to assess the stability of the system and verify that it remained leak-free during and after the crush. We applied two outlier criteria: signal intensity and replication. Only samples with a water yield resulting in a peak area larger than 35 V-s for δ^{H} were considered for the dataset, while any samples with a lower water yield were discarded. For 22 out of 31 samples, it was possible to do two or more analyses with the TC-EA MS technique. Only one sample did not replicate within 1‰ for $\delta^{18}\text{O}$ and was discarded (Supplementary Data Table 1g).

For the CRDS set-up, an online preparation line detailed in ref. ²⁶ is coupled to a Picarro L2140i water isotope analyser. A stable water background of known isotope composition is generated and subtracted from the sample peak, in a similar way to refs. ^{49,50}. For correction purposes, we analysed seven water standards of 0.3 μL before the first sample and five water standards with volumes corresponding to the water yield from the crushed calcites after the last sample. Each of the four samples measured with the CRDS technique was measured twice, replicating within 0.1‰ for $\delta^{18}\text{O}$ (Supplementary Data Table 1g).

For fluid inclusion isotope analysis conducted on both the MS and CRDS systems, the uncertainties are based on the reproducibility reported by ref. ²⁶. In that study, fluid inclusion isotope analysis was conducted on the same TC/EA–MS and CRDS systems that produced the fluid inclusion isotope data for this manuscript. The reproducibility is based on repeated measurements of five samples. For the IRMS system, the reproducibility is 0.4‰ for $\delta^{18}\text{O}$ and 2‰ for δ^{H} (1 s.d.). For the CRDS system, the reproducibility is 0.3‰ for $\delta^{18}\text{O}$ and 1.1‰ for δ^{H} (1 s.d.). These uncertainties compare well with those from several previous fluid inclusion isotope studies using very similar analytical equipment^{40–53}. Where available, replicate analyses are shown individually in the data to indicate the extent to which replication remains within the reproducibility uncertainty. All fluid inclusion $\delta^{18}\text{O}$ and δ^{H} data were normalized to the Vienna Standard Mean Ocean Water–Standard Light Antarctic Precipitation scale by direct comparison with in-house water standards that were directly calibrated against the international standards Vienna Standard Mean Ocean Water and Standard Light Antarctic Precipitation 2.

Dual (Δ_{47} , Δ_{48}) clumped isotope analysis of carbonates. Dual clumped isotope analysis of carbonates (Supplementary Data Table 1c–f) was performed at Goethe University Frankfurt using the analytical set-up described in ref. ²³. Δ_{47} and Δ_{48} data are reported on the Carbon Dioxide Equilibrium Scale at a reaction temperature of 90 °C (CDES 90). For data processing, we followed the CDES 90 correction protocol detailed in ref. ²⁴. It includes (1) correction of m/z 47, 48 and 49 raw intensities for negative backgrounds using scaling factors and intensities measured on the m/z 47.5 cup, (2) correction for scale compression using CO_2 gases equilibrated at 25 °C and 1000 °C, respectively, and (3) correction for subtle long-term variations in Δ_{47} values of reference carbonates ETH 1 and ETH 2. The two samples (JJ0406-312 and JJ0406-690) were analysed between May and August 2019, that is, covering the same period as session 2 in ref. ²⁴. Equilibrated gas data, reference carbonate data, empirically determined scaling factors, empirical transfer functions and temporal Δ_{47} offset functions relevant for sample data correction are, therefore, identical to those reported for session 2 in ref. ²⁴. Background corrected raw data (versus working gas) and final Δ_{47} (CDES, 90 °C) and Δ_{48} (CDES, 90 °C) values of equilibrated gases, reference carbonates and samples are provided in Supplementary Data Table 1d–f. Δ_{47} (CDES, 90 °C) and Δ_{48} (CDES, 90 °C) values obtained for the two samples are (within errors of 2 s.e.) indistinguishable from the equilibrium Δ_{47} (CDES, 90 °C) versus Δ_{48} (CDES, 90 °C) relationship obtained in ref. ²⁴. Temperatures of formation and associated uncertainties were, therefore, calculated from measured Δ_{47} (CDES, 90 °C) values, the equilibrium Δ_{47} (CDES, 90 °C) versus T relationship provided in ref. ²⁴ and 2 s.e. values. All 2 s.e. values are error propagated, considering both the long-term repeatability (2 s.d.) for Δ_{48} (CDES, 90 °C) and Δ_{47} (CDES, 90 °C) measurements of 69.9 and 17.9 ppm, respectively, and the 95% uncertainties associated with the Δ_{48} (CDES, 90 °C) versus T and Δ_{47} (CDES, 90 °C) versus T calibration regression lines²⁴.

Analysis of GDGTs. The procedure to analyse the distribution of glycerol dibiphytanyl glycerol tetraether (GDGT) lipids in the stalagmites from Jiangjun Cave was based on an adaptation of the methods proposed by ref. ²². GDGT measurements (Supplementary Data Table 1b) were performed in the same samples used for fluid inclusion measurements, to maximize the comparability

of temperature estimates with calcite and fluid inclusion $\delta^{18}\text{O}$. After the fluid inclusion measurement, 0.55–1.54 g pulverized material was weighed in a 60 mL cylindrical glass vial. Calcite was subsequently dissolved in 20 mL of 6N HCl and digested on a heating plate at 100 °C for 2 h. After cooling, the digested sample was extracted three times using 20 mL dichloromethane (DCM) in each extraction. The DCM fraction was collected in a 60 mL vial using a 50 mL separation funnel. After the third extraction, 40 μL of C46 GDGT internal standard was added to the extract for GDGT quantification purposes⁵⁴. The solvent was evaporated to complete dryness under nitrogen gas on a heating plate at 45 °C. To remove potential traces of acid and other impurities, the extract was re-dissolved in a mixture of DCM–methanol and passed through a 5% deactivated silica column. The eluate was collected in 4 mL vials, dried, and filtered into a 1 mL vial through a 0.2 μm polytetrafluoroethylene membrane filter using a 1.8% mixture of isopropanol in *n*-hexane. The filtered extracts were analysed using Agilent 1260 Infinity high-performance liquid chromatography (HPLC) coupled to an Agilent 6130 single-quadrupole MS, using a slight adaptation of the method proposed by ref.⁵⁵, as described in ref.⁵⁶.

Cave temperature estimates were obtained by using the recent calibration proposed by ref.²¹

$$\text{Cave air } T = -7.34 + 34.64 \text{ TEX}_{86}$$

The external analytical precision of the method was estimated by analysing a speleothem standard sample prepared by homogenizing around 1 kg of flowstone material from Scladina Cave, Belgium. This standard was analysed at least in duplicate in each batch of samples analysed, obtaining an average cave T of 14.57 °C with a standard deviation of 0.28 °C (1 s.d., $n = 38$). Uncertainties shown in Fig. 2 are 2 s.d. based on the external analytical precision derived from repeated measurements of the speleothem standard (0.56 °C). Due to the limited sample availability, full replicate analysis was only possible in one sample. The s.d. obtained (0.20 °C) is consistent with our estimate from our long-term in-house standard. Calibration uncertainty for speleothem TEX_{86} is ~ 1 °C (2 s.d.) in the temperature range of the samples presented in this study²¹. However, it is important to note that calibration uncertainties mainly affect absolute values not sample-to-sample variability.

The potential effect of crushing and/or heating (to 120 °C) during the fluid inclusion measurement and the cleaning procedure of the crusher on estimated GDGT temperatures was evaluated by performing the fluid inclusion measurement protocol on three samples of our standard speleothem sample from Scladina Cave. The analysis of GDGTs after the fluid inclusion treatment yielded an average T of 14.61 °C with a standard deviation of 0.10 °C (1 s.d., $n = 3$), which is statistically indistinguishable from the T obtained for untreated samples (t test, $P < 0.01$). These results are consistent with the reported stability of TEX_{86} estimates in samples subjected to hydrous pyrolysis at temperatures below 220 °C (ref.⁵⁷).

Calculation of $\delta^{18}\text{O}_p$. Parent water $\delta^{18}\text{O}$ was calculated using water-to-calcite isotope fractionation factors based on the temperature calibration from ref.³⁴, our TEX_{86} temperature data and dual clumped isotope temperatures.

Precipitation map. The map in Fig. 1 was created online with climate explorer (<https://climexp.knmi.nl/start.cgi>) using the CRU TS4.02 dataset⁵⁸.

Data smoothing. Jiangjun $\delta^{18}\text{O}$ and TEX_{86} smoothed loess curve in Fig. 4 was modelled with a smoothing factor of 0.17, and 95% confidence limits were determined by a bootstrapping technique in PAST software⁵⁹.

Data availability

All data produced for this study are available in Supplementary Data 1 and are stored in the data repository of the National Oceanic and Atmospheric Administration. Other source data for Figs. 2–4 and Extended Data Figs. 3–4 are referenced in the Source data provided with this paper.

Code availability

This research paper has no associated code.

References

- Luo, W., Wang, S. & Xie, X. A comparative study on the stable isotopes from precipitation to speleothem in four caves of Guizhou, China. *Geochemistry* **73**, 205–215 (2013).
- Edwards, R. L., Chen, J. H. & Wasserburg, G. J. ^{238}U – ^{234}U – ^{230}Th – ^{232}Th systematics and the precise measurement of time over the past 500,000 years. *Earth Planet. Sci. Lett.* **81**, 175–192 (1987).
- Cheng, H. et al. Improvements in ^{230}Th dating, ^{230}Th and ^{234}U half-life values, and U–Th isotopic measurements by multi-collector inductively coupled plasma mass spectrometry. *Earth Planet. Sci. Lett.* **371**, 82–91 (2013).
- Jaffey, A. H., Flynn, K. F., Glendenin, L. E., Bentley, W. C. & Essling, A. M. Precision measurement of half-lives and specific activities of ^{235}U and ^{238}U . *Phys. Rev. C* **4**, 1889–1906 (1971).

- Scholz, D. & Hoffmann, D. L. StalAge - an algorithm designed for construction of speleothem age models. *Quat. Geochronol.* **6**, 369–382 (2011).
- Vonhof, H. et al. High-precision stable isotope analysis of $<5 \mu\text{g}$ CaCO_3 samples by continuous-flow mass spectrometry. *Rapid Commun. Mass Spectrom.* **34**, e8878 (2020).
- Plessen, B. & Lüders, V. Simultaneous measurements of gas isotopic compositions of fluid inclusion gases (N_2 , CH_4 , CO_2) using continuous-flow isotope ratio mass spectrometry. *Rapid Commun. Mass Spectrom.* **26**, 1157–1161 (2012).
- Vonhof, H. B. et al. A continuous-flow crushing device for on-line $\delta^2\text{H}$ analysis of fluid inclusion water in speleothems. *Rapid Commun. Mass Spectrom.* **20**, 2553–2558 (2006).
- Dassié, E. P. et al. A newly designed analytical line to examine fluid inclusion isotopic compositions in a variety of carbonate samples. *Geochem. Geophys. Geosyst.* **19**, 1107–1122 (2018).
- Affolter, S., Fleitman, D. & Leuenberger, D. New online method for water isotope analysis of speleothem fluid inclusions using laser absorption spectroscopy (WS-CRDS). *Clim. Past* **10**, 1291–1304 (2014).
- Labuhn, I. et al. A high-resolution fluid inclusion $\delta^{18}\text{O}$ record from a stalagmite in SW France: modern calibration and comparison with multiple proxies. *Quat. Sci. Rev.* **110**, 152–165 (2015).
- Dublyansky, Y. V. & Spötl, C. Hydrogen and oxygen isotopes of water from inclusions in minerals: design of a new crushing system and on-line continuous-flow isotope ratio mass spectrometric analysis. *Rapid Commun. Mass Spectrom.* **23**, 2605–2613 (2009).
- Affolter, S. et al. Central Europe temperature constrained by speleothem fluid inclusion water isotopes over the past 14,000 years. *Sci. Adv.* **5**, eaav3809 (2019).
- Huguet, C. et al. An improved method to determine the absolute abundance of glycerol dibiphytanyl glycerol tetraether lipids. *Org. Geochem.* **37**, 1036–1041 (2006).
- Hopmans, E. C., Schouten, S. & Sinninghe Damsté, J. S. The effect of improved chromatography on GDGT-based palaeoproxies. *Org. Geochem.* **93**, 1–6 (2016).
- Auderset, A., Schmitt, M. & Martínez-García, A. Simultaneous extraction and chromatographic separation of *n*-alkanes and alkenones from glycerol dialkyl glycerol tetraethers via selective accelerated solvent extraction. *Org. Geochem.* **143**, 103979 (2020).
- Schouten, S., Hopmans, E. C. & Sinninghe Damsté, J. S. The effect of maturity and depositional redox conditions on archaeal tetraether lipid palaeothermometry. *Org. Geochem.* **35**, 567–571 (2004).
- Harris, I., Jones, P. D., Osborn, T. J. & Lister, D. H. Updated high-resolution grids of monthly climatic observations – the CRU TS3.10 dataset. *Int. J. Climatol.* <https://doi.org/10.1002/joc.3711> (2013).
- Hammer, O., Harper, D. A. T. & Ryan, P. D. PAST: paleontological statistics software package for education and data analysis. *Palaeontol. Electron.* **4**, 1–9 (2001).
- Peterson, T. C. & Vose, R. S. An overview of the Global Historical Climatology Network temperature database. *Bull. Am. Meteorol. Soc.* **78**, 2837–2850 (1997).
- Lawrimore, J. H. et al. An overview of the Global Historical Climatology Network monthly mean temperature data set, version 3. *J. Geophys. Res. Atmos.* <https://doi.org/10.1029/2011jd016187> (2011).
- Durre, I., Menne, M. J. & Vose, R. S. Strategies for evaluating quality assurance procedures. *J. Appl. Meteorol. Climatol.* **47**, 1785–1791 (2008).
- The Global Network of Isotopes in Precipitation Database* (IAEA/WMO, 2019); <https://nucleus.iaea.org/wiser>
- Li, T. Y. et al. Stalagmite-inferred variability of the Asian summer monsoon during the penultimate glacial–interglacial period. *Clim. Past* **10**, 1211–1219 (2014).
- Kelly, M. J. et al. High resolution characterization of the Asian monsoon between 146,000 and 99,000 years B.P. from Dongge Cave, China and global correlation of events surrounding Termination II. *Palaeogeogr. Palaeoclimatol. Palaeoecol.* **236**, 20–38 (2006).
- Wang, Y. J. et al. Millennial- and orbital-scale changes in the East Asian monsoon over the past 224,000 years. *Nature* **451**, 1090–1093 (2008).

Acknowledgements

The authors thank S. Brömmle for conducting CaCO_3 oxygen isotope analysis and M. Schmidt for technical support in the TEX_{86} analysis at the MPIC. This study was funded by the Max Planck Society. H.C. acknowledges funding from NSFC grant 41888101, and R.L.E. acknowledges US NSF grant 1702816. J.A.W. acknowledges support from the Institute for Basic Science (IBS), Republic of Korea, under IBS-R028-Y2.

Author contributions

G.H.H., H.B.V., J.A.W., A.M.-G. and H.C. designed the project. X.L., L.S., Y.T., H.Z. and J.A.W. performed the U series dating. J.A.W. conducted the fluid inclusion isotope

analysis with support from H.B.V. P.-R.E conducted the GDGT analysis supervised by A.M.-G. and J.F. conducted the dual clumped isotope analysis. J.A.W. wrote the manuscript with support from H.B.V. and A.M.-G. All authors contributed to the manuscript at various stages.

Funding

Open access funding provided by Max Planck Society.

Competing interests

The authors declare no competing interests.

Additional information

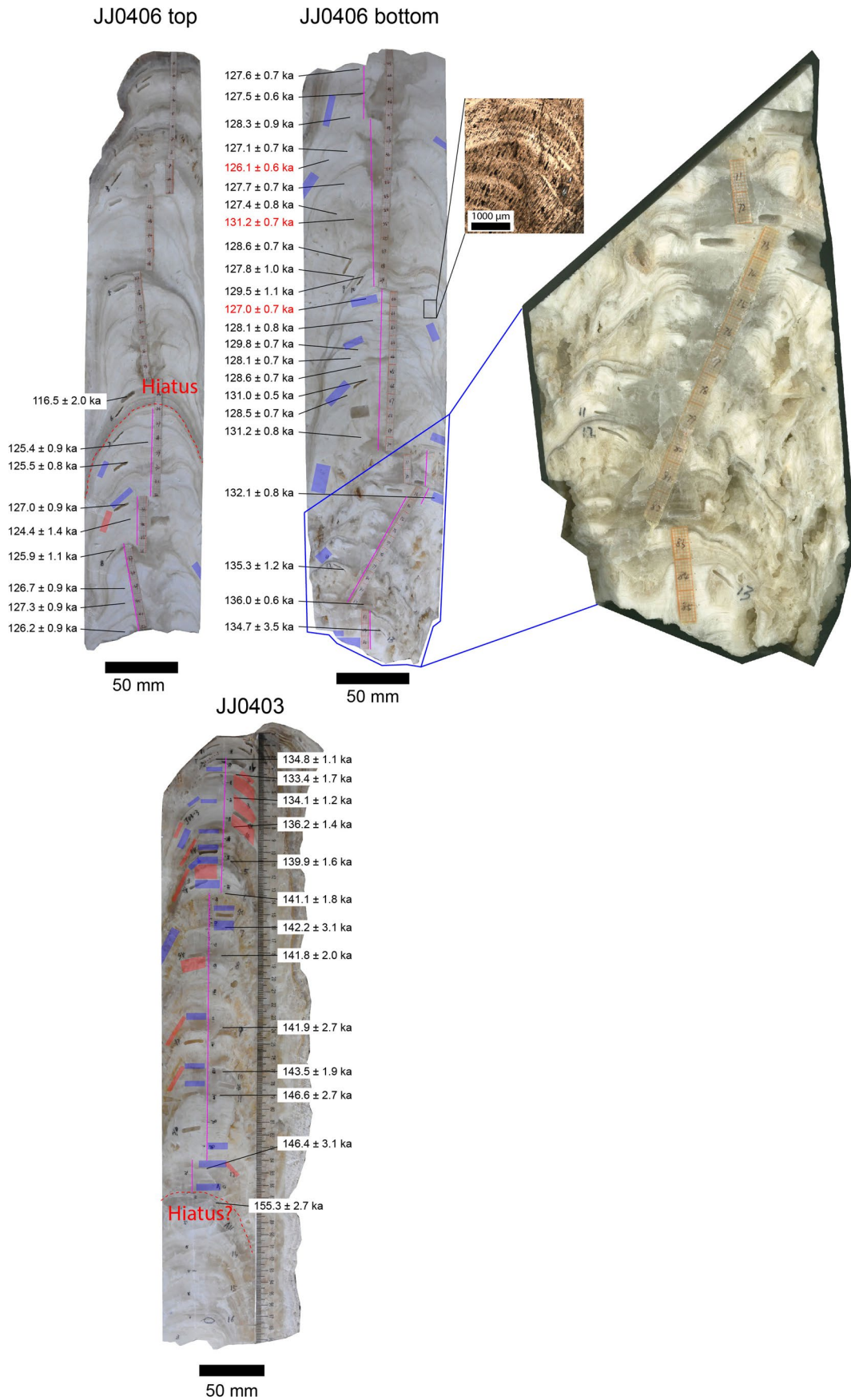
Extended data is available for this paper at <https://doi.org/10.1038/s41561-021-00851-9>.

Supplementary information The online version contains supplementary material available at <https://doi.org/10.1038/s41561-021-00851-9>.

Correspondence and requests for materials should be addressed to Jasper A. Wassenburg.

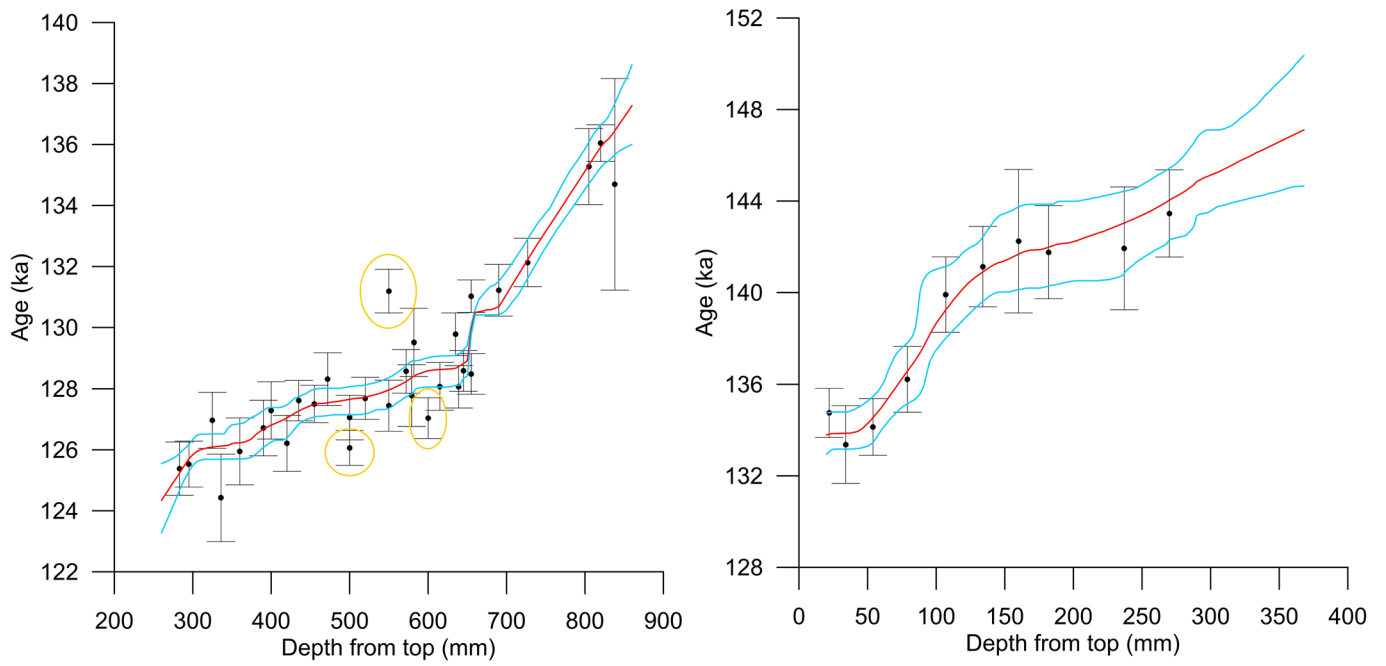
Peer review information *Nature Geoscience* thanks Vasile Ersek and the other, anonymous, reviewer(s) for their contribution to the peer review of this work. Primary Handling Editor(s): James Super.

Reprints and permissions information is available at www.nature.com/reprints.

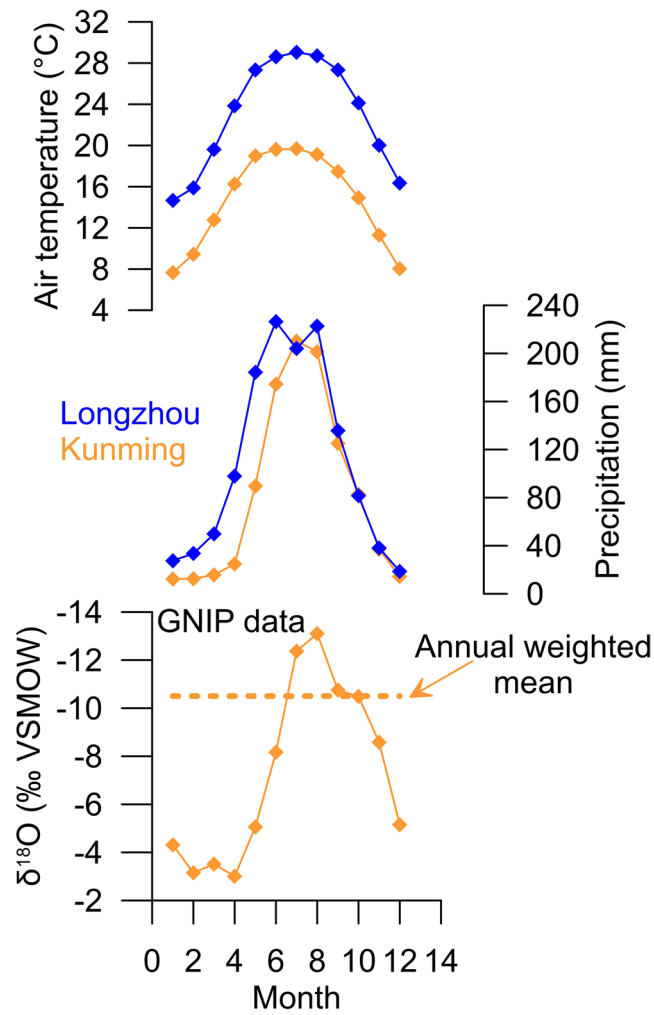


Extended Data Fig. 1 | See next page for caption.

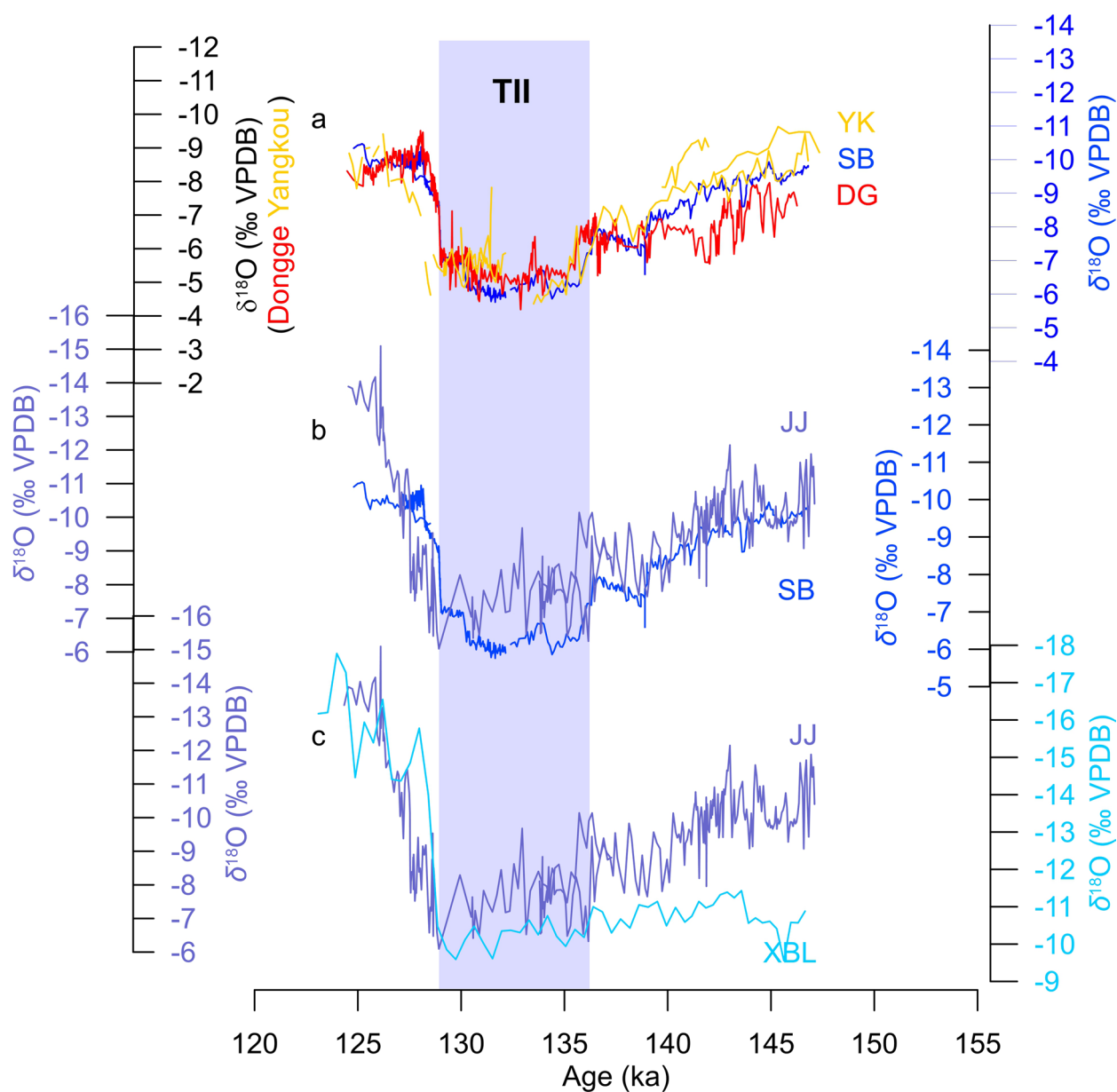
Extended Data Fig. 1 | Sampling positions. Positions of $^{230}\text{Th}/\text{U}$ dating, oxygen isotope transect (magenta), fluid inclusions (blue) and TEX_{86} analysis for which the crush residue did not provide enough material for one analysis (red) are indicated. Thin section under polarization microscope of calcite with fluid inclusions is shown for speleothem JJ0406. The bottom part of JJ0406 zoomed in on the right shows the most pronounced pool structure at the growth axis and dissolution features indicating the lowest drip water saturation indices.



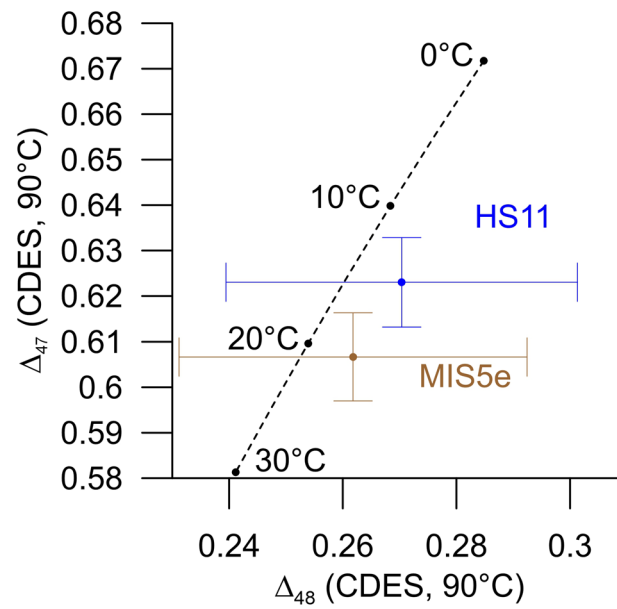
Extended Data Fig. 2 | Age depth models with $^{230}\text{Th}/\text{U}$ datings and 2σ uncertainties. Left: speleothem JJ0406, right: speleothem JJ0403. Three outliers were detected by StalAge⁴⁵ for JJ0406, which are indicated by the yellow circles.



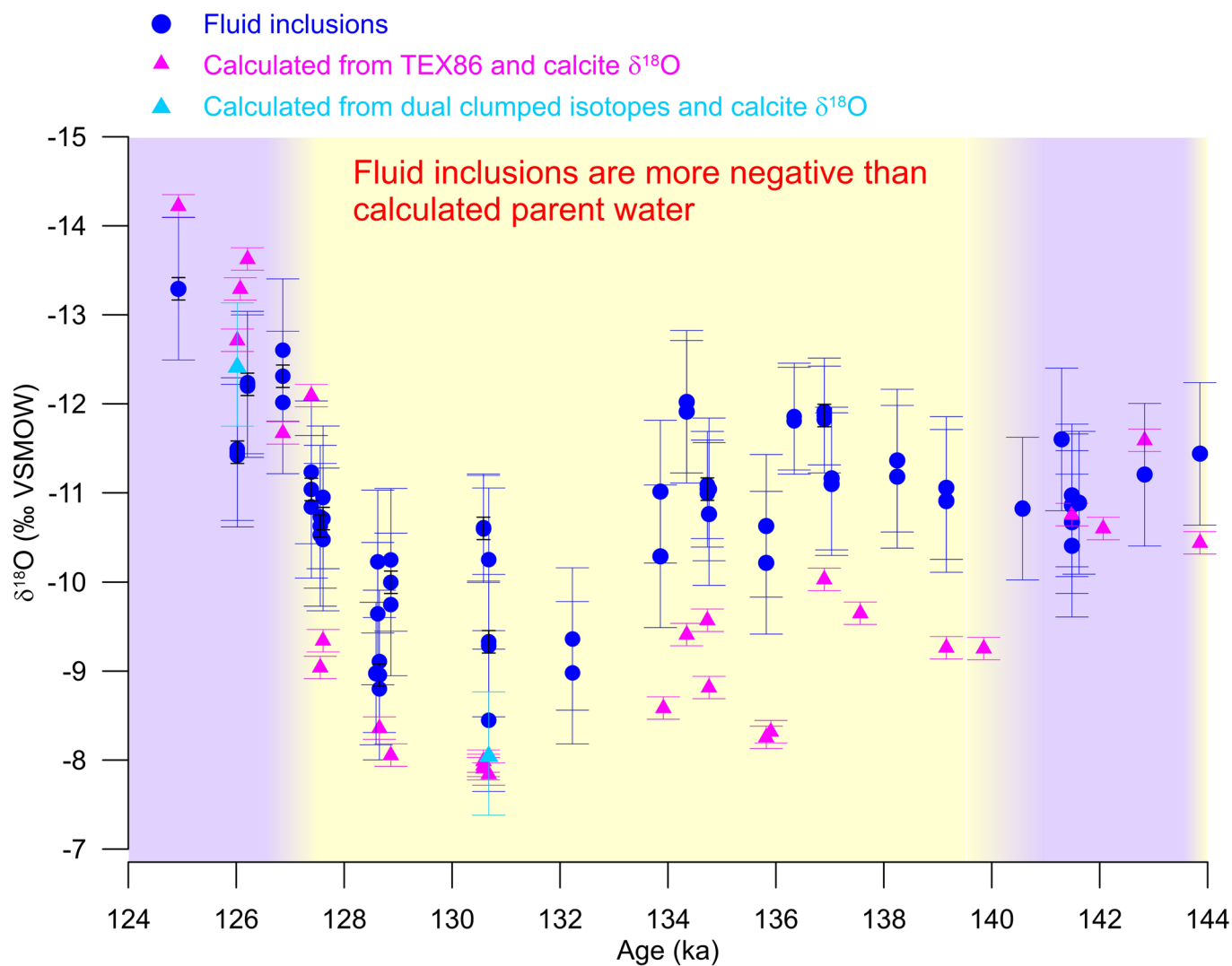
Extended Data Fig. 3 | Seasonal cycles study site. Air temperature (top), precipitation (middle)⁶⁰⁻⁶² and the isotope composition of meteoric rainfall (bottom)⁶³. Kunming and Longzhou are in the vicinity of Jiangjun Cave. Annual weighted mean value for the oxygen isotope compositions at Kunming is indicated by the dashed line.



Extended Data Fig. 4 | Speleothem $\delta^{18}\text{O}_{\text{e}\text{e}}$ records. Yangkou⁶⁴ (YK), Dongge^{18,65} (DG) and Sanbao^{10,66} (SB) Caves represent the East Asian Monsoon region (a). Jiangjun (JJ) versus Sanbao Caves (b). Jiangjun²⁷, and Xiaobailong³¹ (XBL) Cave represent the Indian Monsoon (IM) region (c). The purple bar indicates the timing of Termination II (TII).



Extended Data Fig. 5 | Dual clumped isotope data. Δ_{47} versus Δ_{48} for MIS5e and HS11 with respect to the temperature equilibrium line following ref. ²⁴. The calcite precipitated indistinguishable from equilibrium and temperatures derived from the dual clumped isotope analysis are within error of our TEX_{86} temperature reconstruction. Uncertainties are 2SE.



Extended Data Fig. 6 | Calculated parent water versus fluid inclusion $\delta^{18}\text{O}$. Calculated $\delta^{18}\text{O}_p$ values are based on TEX86 and dual clumped isotope temperatures and $\delta^{18}\text{O}_{\text{Cc}}$ using the $\delta^{18}\text{O}$ temperature calibration from ref. ³⁴. $\delta^{18}\text{O}_{\text{FI}}$ and calculated $\delta^{18}\text{O}_p$ are consistent, but $\delta^{18}\text{O}_{\text{FI}}$ is about 1–3 ‰ more negative from 139 ka to 127.5 ka. Uncertainties are 2 SD for fluid inclusions and TEX₈₆ based parent water $\delta^{18}\text{O}$, and 2SE for dual clumped isotope based parent water $\delta^{18}\text{O}$.